

Towards systematically improvable models for actinides in condensed phase: the electronic spectrum of uranyl in $\text{Cs}_2\text{UO}_2\text{Cl}_4$ as a test case†

Cite this: *Phys. Chem. Chem. Phys.*, 2013, **15**, 15153

André Severo Pereira Gomes,^{*a} Christoph R. Jacob,^{*b} Florent Réal,^a Lucas Visscher^c and Valérie Vallet^a

In this work we explore the use of frozen density embedding [Gomes *et al.*, *Phys. Chem. Chem. Phys.*, 2008, **10**, 5353] as a way to construct models of increasing sophistication for describing the low-lying electronic absorption spectra of UO_2^{2+} in the $\text{Cs}_2\text{UO}_2\text{Cl}_4$ crystal. We find that a relatively simple embedding model, in which all but the UO_2^{2+} unit are represented by an embedding potential, can already describe the main spectral features and the main environment effects can be attributed to the four chloride ions situated at the UO_2^{2+} equatorial plane. Contributions from species further away, albeit small, are found to be important for reaching a close agreement with experimentally observed quantities such as the excited states' relative positions. These findings suggest that such an embedding approach is a viable alternative to supermolecular calculations employing larger models of actinyl species in condensed phase. Nevertheless, we observe a slight red shift of the excitation energies calculated with our models compared to experimental results, and attribute this discrepancy to inaccuracies in the underlying structural parameters.

Received 17th May 2013,
Accepted 11th July 2013

DOI: 10.1039/c3cp52090k

www.rsc.org/pccp

1 Introduction

Optical spectroscopy is a powerful probe of the interactions between the constituents of molecular complexes containing actinide species, as well as the interaction of such complexes and their surroundings. However, actinide species are often difficult to manipulate due to their radiotoxicity and may present rather complicated spectra. Therefore, the interpretation of experimental results is greatly helped by the use of theoretical models that provide detailed information on the electronic structure. This may, for instance, aid in deconvoluting the measured spectra in solution into the contributions of different species that may coexist in equilibrium.^{1,2}

Theoretical (semi)empirical approaches based upon crystal or ligand-field theory^{3–5} provide a simple physical picture based

on effective Hamiltonians. This makes such methods the first choice for the interpretation of experimental results. However, as their accuracy depends on the validity of the simple model and the quality of the experimental data used in the parametrization, their predictive power is limited.

The computationally much more demanding *ab initio* electronic structure approach^{6–8} based on wavefunction theory (WFT) or density functional theory (DFT) can, for small models, provide accurate non-empirical data for small model systems. This was demonstrated by a number of studies over the past two decades.^{9–30} However, such studies also demonstrate that the accurate prediction of the energies of electronically excited states is a very demanding task. Often, one passes from a relatively simple, closed-shell ground state to excited states which have contributions from several close-lying open-shell configurations. This makes the balanced treatment of ground and excited states difficult and may give rise to substantial errors in the calculated transition energies. Fortunately, one often finds that differential correlation effects for excited states of similar character are smaller, so that their relative energies can be described with less effort than absolute ones.

These difficulties are illustrated in the case of the actinyl(vi) and (v) ions ($\text{AnO}_2^{2+/+}$, An = U, Np, Pu, Am), which are very stable species that are found both in the gas and in the condensed phases (in particular in solution).³¹ For those systems, it is well-established³¹ that the low-lying excited states arise from

^a Université de Lille 1, Laboratoire PhLAM, CNRS UMR 8523, CNRS FR 2416, Bât P5, F-59655 Villeneuve d'Ascq Cedex, France.

E-mail: andre.gomes@univ-lille1.fr; Fax: +33 3 2033 7020; Tel: +33 3 2043 4980

^b Karlsruhe Institute of Technology (KIT), Center for Functional Nanostructures and Institute of Physical Chemistry, Wolfgang-Gaede-Str. 1a, 76131 Karlsruhe, Germany. E-mail: christoph.jacob@kit.edu

^c Amsterdam Center for Multiscale Modeling, Department of Theoretical Chemistry, Faculty of Sciences, Vrije Universiteit Amsterdam, De Boelelaan 1083, 1081 HV Amsterdam, Netherlands. E-mail: l.visscher@vu.nl

† Electronic supplementary information (ESI) available. See DOI: 10.1039/c3cp52090k

excitations to unoccupied non-bonding ($5f_{\delta}$, $5f_{\phi}$) actinide orbitals from the (i) actinyl bonding orbitals (for $An = U(vi)$), in internal uranyl ligand-to-metal charge-transfer (LMCT) excitations; and from the (ii) partially filled f (for $An = U(v)$, Np, Pu, Am), in the so-called f–f transitions. Somewhat higher in energy one also finds (iii) LMCT transitions from ligands bound in the equatorial plane. The latter, even when not significantly contributing to excitations of types (i) and (ii), can affect their energies and oscillator strengths.^{32,33} This makes the description of these nearest ligands essential in investigations on condensed phases, while also second-nearest neighbors such as outer solvation shells can still differentially affect electronic states (*via*, *e.g.*, hydrogen bonding or by aggregation³⁴).

For the investigation of excitations of types (i)–(iii) with WFT methods employing many-electron model spaces (*e.g.*, CAS or RAS)^{16,24} consideration of just the equatorial ligands directly bound to the actinyls is already at the limit of what is computationally feasible. A more approximate treatment of the excitations from the ligands^{16,19,35} is therefore often attempted to reduce the computational cost. In addition, idealized geometries are used to make as much use of symmetry as possible. Time-dependent DFT (TD-DFT) approaches offer a computationally less demanding alternative, but are often considered as too inaccurate for actinyl systems due to the known tendency of most available exchange–correlation functionals to spuriously stabilize delocalized charges.^{36–39} Recent studies^{17,18} using the CAM-B3LYP⁴⁰ functional indicated that range-separated hybrid functionals may yield quantitatively correct spectra for uranyl complexes. Nevertheless, (TD-)DFT remains inapplicable to f–f spectra (*i.e.*, excitations of type (ii)) because of the multireference character of the ground states.

A way to overcome the size restriction for WFT approaches is to resort to embedding techniques⁴¹ such as the frozen density embedding (FDE) method.^{42,43} With FDE, a large system is partitioned into smaller subsystems interacting through a so-called embedding potential. This embedding potential is determined from the densities of the individual subsystems. The subsystems can then be treated exclusively with DFT (DFT-in-DFT),^{44–49} or one (or a few) subsystems can be treated with WFT (WFT-in-DFT),^{50–55} depending on the balance between computational cost and accuracy one wishes to achieve. An interesting aspect of FDE is that, by retaining a fully quantum mechanical description for all subsystems, both ground and excited state properties for the whole system remain in principle accessible.^{56–59} This has led to the development of efficient, DFT-based protocols to investigate the coupling of localized electronic excitations in large systems.^{60–62}

Some of us have previously employed WFT-in-DFT embedding to study the f–f spectrum [*i.e.*, excited states of type (ii)] of NpO_2^{2+} as an impurity in a $Cs_2UO_2Cl_4$ crystal,⁵³ using FDE to construct a (frozen) model for the crystal environment surrounding a central neptunyl (NpO_2^{2+}) or neptunyl tetrachloride ($NpO_2Cl_4^{2-}$) unit. Subsequently, some of us have applied DFT-in-DFT and WFT-in-DFT embedding to investigate the low-lying excited states of the CUO molecule, which is isoelectronic to UO_2^{2+} , surrounded by noble gas atoms in its equatorial plane.⁶³ These excited

states are of type (i), *i.e.*, internal LMCT-type excitations. While for these LMCT-type excitations in CUO it turned out that the limited accuracy of the (orbital-free) kinetic energy functionals prevented an accurate description of the noble-gas actinide species already for the ground state, we have found for the f–f spectrum of NpO_2^{2+} that a simple embedding model where the chlorides are represented by an FDE embedding potential did yield accurate results. This is due to the intrinsically localized nature of f–f transitions where ground and low-lying excited states are dominated by molecular spinors with strong contributions from Np-centered 5f spinors. These previous findings raise the question to what extent actinyl spectra can be modeled with WFT-in-DFT embedding approaches, and what accuracy can be reached using the minimal model discussed above for excitations other than f–f excitations.

Thus, our aim in this paper is to further evaluate the performance of FDE-based embedding schemes by investigating the spectra of uranyl tetrachloride ($UO_2Cl_4^{2-}$). This species is known to play a key role in pyroprocessing techniques of the spent nuclear fuels due to the use of high-temperature chloride melts.⁶⁴ There is a wealth of accurate experimental spectra available both for the $Cs_2UO_2Cl_4$ crystal^{65–68} and for $UO_2Cl_4^{2-}$ in non-aqueous solvents^{69,70} and in the gas phase.⁷¹ We believe that calculating the spectra of UO_2^{2+} in $Cs_2UO_2Cl_4$ represents an interesting test for subsystem models since the low-lying transitions are again of type (i), with potentially important contributions from the ligand to the occupied orbitals involved. Moreover, it presents an opportunity to further investigate the performance of different electronic structure methods in conditions that closely mimic those of experiments. Of all previous *ab initio* studies,^{10,18–20,71,72} only the one by Matsika and Pitzer¹⁰ calculated the spectrum with the inclusion of a model for the crystal environment.

2 Computational methods

All electronic spectra calculations were performed at the experimental X-ray structure⁷³ (see Section 3.1 for details) with a development version of the DIRAC electronic structure code⁷⁴ (revision ab65b36), employing Dyal's basis sets⁷⁵ of triple-zeta quality for uranium, and Dunning's aug-cc-pVTZ sets⁷⁶ for oxygen and chlorine, all of which are left uncontracted.

The Dirac–Coulomb (DC) Hamiltonian was used throughout, along with the usual approximation of the (SS|SS)-type integrals by a point charge model.⁷⁷ In (TD-)DFT calculations the CAM-B3LYP⁴⁰ functional was used, whereas the WFT approach employed here is the intermediate Hamiltonian Fock-space coupled cluster method (IHFSCSD),^{78–81} which allows for a proper description of a possible multiconfigurational nature of excited states.

In the IHFSCSD calculations the excitation energies were obtained with the (1h,1p) sector of Fock-space, meaning that in the process electron attachment and ionization energies were also calculated *via* the (0h,1p) and (1h,0p) sectors of Fock-space, respectively. For cases in which we have not been able to obtain solutions for the (1h,1p) sector due to the presence of

intruder states, we have resorted to an approximate treatment of the CC amplitudes in this sector, which are determined in a manner akin to that of MP2 – in practice by performing a single CC iteration for the (1h,1p) sector after having converged the preceding sectors. We shall here denote this approach by the IHFSCC-112 acronym.

Due to computational constraints we are forced to truncate the virtual space in the WFT calculations. In order to verify the effect of this truncation, we have explored three different correlating (Q) spaces by considering all uranyl spinors with energies between (1) -6.0 and 5.0 a.u.; (2) -6.0 and 12.0 a.u.; and (3) -6.0 and 100.0 a.u. This way, the occupied $5d$ spinors are always correlated (yielding a total of 34 correlated electrons), with up to 446 virtual spinors. The IHFS model (P) spaces were the same for all correlation spaces. These are slightly modified compared to those employed in prior work,^{17,27} and contain at least the $6d$ and $5f$ spinors. More details on the definition of the P and Q spaces can be found in Table 1. Information on the computational cost of these calculations can be found in Table S1 in the ESI.†

We note that we were not able to obtain a Fock-space reference spectrum for uranyl tetrachloride, due to difficulties in performing calculations with the large active spaces required to take into account the ligand (occupied and virtual) spinors that have energies in between the occupied and virtual spinors involved in the excitations.

DFT-in-DFT embedding calculations^{42,44,47} were performed with the ADF⁸² code *via* the PyADF scripting environment.⁸³ In the calculations, the spin-free (SF) ZORA^{84,85} Hamiltonian was used along with the corresponding TZ2P basis sets⁸⁶ for uranium, oxygen, and chlorine. We have employed the SAOP^{87–89} model potential for the active subsystems, whose densities were

allowed to relax through the freeze–thaw procedure until convergence (reached within 20 iterations). The non-additive exchange–correlation and kinetic-energy contributions to the embedding potential were calculated with the PW91⁹⁰ exchange–correlation and PW91k⁹¹ kinetic energy functionals, respectively. The integration accuracy parameter in ADF was set to 10. The DFT-in-DFT embedding potentials obtained with ADF and PyADF were subsequently used in Dirac calculations as effective one-electron operators according to the “static” embedding scheme outlined in ref. 53.

3 Results and discussion

3.1 Models for uranyl in $\text{Cs}_2\text{UO}_2\text{Cl}_4$

Our main goal in this work is to explore the construction of models of increasing complexity that can describe the absorption spectra of $\text{Cs}_2\text{UO}_2\text{Cl}_4$. In this crystal, whose structure has been accurately determined from X-ray diffraction studies,⁷³ the uranyl cation is surrounded by four chlorine atoms. These are oriented along the equatorial plane, but show a C_{2h} site symmetry, as the O–U–O axis intersects the plane defined by the four chlorides with a slight deviation from 90° . The U–O and U–Cl distances are 1.774 Å and 2.671 Å, respectively. Further away from the uranium one finds a shell of cesium atoms at ≈ 4.6 Å from the central uranium, and the nearest uranium atom at ≈ 5.8 Å. Therefore, the crystal is made up of well-separated uranyl tetrachloride ($\text{UO}_2\text{Cl}_4^{2-}$) units interspersed with cesium ions.

The simplest models are (a) the bare UO_2^{2+} ion and (d) the $\text{UO}_2\text{Cl}_4^{2-}$ unit, as shown in Fig. 1. In addition, one can consider intermediate models in which only the uranyl species is treated explicitly while the equatorial ligands are included in an approximate fashion. This could be achieved either (b) by a simple point-charge embedding⁴¹ or (c) by using an FDE-based embedding potential.⁵³ For all four models, we use an idealized structure with D_{4h} symmetry instead of the C_{2h} point group corresponding to the crystal's site symmetry. This will simplify our analysis and allow for a direct comparison to calculations in the literature. In the calculations, only the Abelian point group D_{2h} can be used (instead of D_{4h}) and, therefore, the irreducible representations of D_{2h} are used to label the excited states in our tables.

More sophisticated models, shown in Fig. 2, extend those above and include effects arising from the long-range interactions with the crystal lattice. The structure of the crystal

Table 1 IHFSCSD main model (P_m), intermediate model space (P_i) and correlation (Q) spaces employed for the different models for the environment surrounding the UO_2^{2+} species, given in terms of number of spinor pairs of gerade (ungerade) symmetry in each subspace. The “h” and “p” superscripts denote “holes” and “particles”, respectively

Model	Environment	P_1^h	P_m^h	P_m^p	P_i^p	Q^h	Q^p	
(a)	None	Q_2	2 (4)	3 (3)	5 (10)	6 (7)	5 (0)	101 (93)
(b)	Cl_4^{4-} p.c.	Q_2	2 (4)	3 (3)	7 (13)	9 (10)	5 (0)	101 (93)
(c)	Cl_4^{4-} FDE	Q_1	2 (4)	3 (3)	7 (13)	9 (10)	5 (0)	72 (58)
		Q_2						101 (93)
		Q_3						122 (128)
(e), (f)	$\text{Cs}_2\text{UO}_2\text{Cl}_4$	Q_1	2 (4)	3 (3)	7 (13)	9 (10)	5 (0)	72 (58)

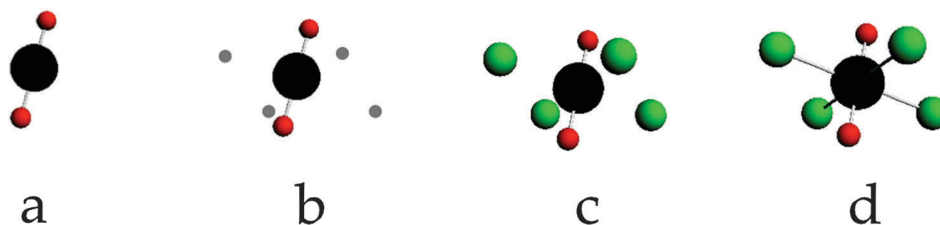


Fig. 1 Models without the crystal environment: (a) the bare uranyl species; (b) uranyl with point-charge embedding; (c) uranyl with FDE embedding; and (d) the uranyl chloride species (uranium: black; oxygen: red; chlorine: green; point charges: grey).

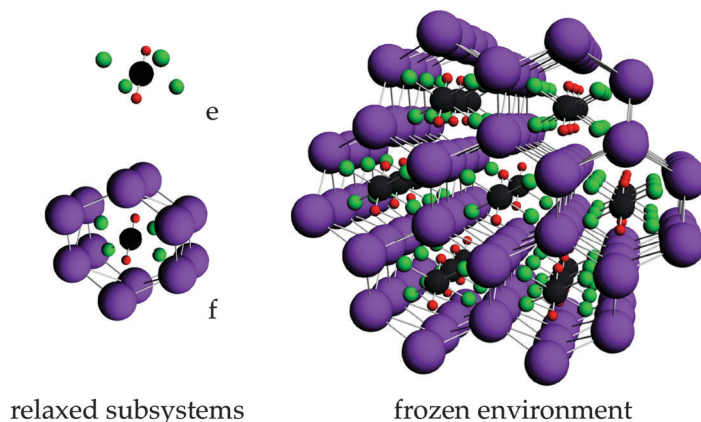


Fig. 2 Uranyl FDE embedding models including the crystal environment (shown on the right), where one relaxes (e) only the nearest chlorides; (f) the nearest chlorides and 12 cesium ions (uranium: black; oxygen: red; cesium: purple; chlorine: green).

suggests a natural subdivision of $\text{Cs}_2\text{UO}_2\text{Cl}_4$ into three distinct regions – an inner one containing the core model(s) above, an intermediate one containing at least the shell of the nearest cesium atoms, and finally the remainder of the crystal. Our first model (e) is built using the same strategy as in ref. 53. The basic representation of the crystal environment is the combination of the intermediate region (comprising 20 $\text{UO}_2\text{Cl}_4^{2-}$ and 90 Cs^+ ions) around the central unit and an array of point charges is defined to represent the Madelung potential due to the rest of the crystal.⁹² The electron density of the intermediate region, which is necessary to determine the corresponding FDE embedding potential, is obtained as the sum of the densities from DFT calculations (SAOP/TZP) on the isolated ($\text{UO}_2\text{Cl}_4^{2-}$ and Cs^+) species. In a more refined model (f) the density for the 12 cesium ions nearest to the uranyl species was allowed to relax through a DFT-in-DFT freeze-and-thaw procedure. Both models (e) and (f) are derived from the experimental crystal structure, in which the central uranyl unit only has C_{2h} symmetry.

3.2 Assessing the models without a crystal environment

First, we consider the models without the crystal environment. To assess the accuracy that can be achieved with these models, we will compare the electronic spectrum of uranyl tetrachloride (model d) to those obtained with the approximate models (a), (b) and (c) (see Fig. 1).

3.2.1 The electronic structure of $\text{UO}_2\text{Cl}_4^{2-}$. Before discussing the approximate models, we recall some key findings from calculations on uranyl tetrachloride.^{10,16,18–20,71} First, theoretical and experimental^{31,65} works assign the spectrum below $\approx 30\,000\text{ cm}^{-1}$ to excitations local to the uranyl species [*i.e.*, excitations of type (i) in the classification introduced above]. These involve the highest occupied *ungerade* orbital and part of the virtual uranium f manifold. LMCT from the chloride ligands [*i.e.*, excitations of type (iii)] occurs at somewhat higher energy and concerns excitations from essentially pure chloride ligand orbitals.^{31,71} This reflects the fact that the U–Cl bonds, on the basis of experimental results and Mulliken population analyses from correlated wavefunctions,¹⁹ are considered to be largely ionic and have only weak covalent character. Recent AIM

studies^{93,94} corroborate this picture, although the experimentally determined densities used in ref. 93 seem to indicate somewhat stronger covalency. One should keep in mind, however, that this is not an intrinsic characteristic of U–Cl bonds; for instance, in compounds not containing the actinyl group such as metallocene dichlorides, there is evidence that U–Cl covalency can be substantial.⁹⁵

Rather good agreement is found¹⁸ between WFT and DFT calculations with the CAM-B3LYP exchange–correlation functional, with a few notable exceptions: CAM-B3LYP reorders some states (in D_{4h} notation) with respect to CASPT2^{16,19} as well as to the experimental assignment. In particular, the first B_{1g} and B_{2g} states (both of $\sigma_{1/2u} \rightarrow f_\phi$ character) and the second B_{1g} and B_{2g} states (both of $\sigma_{1/2u} \rightarrow f_\delta$ character) are each interchanged. Apart from these discrepancies, there is also a crossing between the first E_g (of $\sigma_{1/2u} \rightarrow f_\delta$ character) and B_{1g} (for CAM-B3LYP)/ B_{2g} (CASPT2) states found at a U–O distance of $\approx 1.83\text{ \AA}$ for the former and of $\approx 1.86\text{ \AA}$ for the latter.

3.2.2 Approximate models, DFT. Proceeding now with an analysis of the simplest models (a–c), we take the CAM-B3LYP results for model (d), *i.e.*, the full uranyl tetrachloride, as the reference. All values are given in Table 2, where we order the electronic states according to the experimental classification.^{31,65} We note that the experimental excitation energies for the twelve

Table 2 CAM-B3LYP excitation energies (columns “abs.”) in wavenumbers for different uranyl models (a–c) and uranyl chloride (model d), without the presence of the crystal environment ($r_{\text{U–O}} = 1.774\text{ \AA}$). The energies relative to the first excited state are also shown (columns “rel.”)

State	Label (D_{2h})	Model (a)		Model (b)		Model (c)		Model (d)	
		abs.	rel.	abs.	rel.	abs.	rel.	abs.	rel.
I, II	B_{2g}, B_{3g}	13 215		17 265		18 115		19 018	
III	B_{1g}	11 805	–1410	16 341	–924	18 321	206	19 934	917
IV	A_g	11 805	–1410	16 239	–1026	17 981	–134	19 288	270
V, VI	B_{2g}, B_{3g}	15 135	1920	17 681	416	19 565	1451	20 970	1952
VII	A_g	17 084	3869	19 394	2129	20 539	2424	21 745	2728
VIII	B_{1g}	17 084	3869	19 660	2395	20 829	2714	21 592	2574
IX, X	B_{2g}, B_{3g}	20 461	7246	23 424	6159	24 747	6633	25 531	6513
XI	B_{1g}	18 896	5681	23 875	6610	26 137	8022	27 058	8040
XII	A_g	18 896	5681	23 876	6611	26 140	8025	27 112	8094

lowest excited states discussed in this paper can be found in Table 5.

Model (a), the isolated uranyl unit, is obviously the least suitable model and places states III and IV below the doubly degenerate (I–II) first excited state of uranyl tetrachloride. In addition, the relative order of the highest states (IX, X vs. XI and XII) is different relative to the reference model (d). The strong red shift ($\approx 7000 \text{ cm}^{-1}$) of all states with respect to model (d) can be easily understood: the isolated uranyl cation has a much shorter bond length so that at $r_{\text{U-O}} = 1.774 \text{ \AA}$ the ground and excited states—which have longer bond lengths—are calculated to have a very small energy gap. The great sensitivity of the vertical excitation energies to the bond length for this system is also evident if our results for model (d) are compared to those of Tecmer *et al.*¹⁸ With the shorter bond length of $r_{\text{U-O}} = 1.764 \text{ \AA}$ used in this study, the excitation energies are $1000\text{--}3000 \text{ cm}^{-1}$ higher than the one found here.

These flaws of the simplest model are considerably reduced in the point-charge embedding model (b). The lowest four states still resemble the spectrum for the isolated species. In particular, the ordering of the states is at odds with that for uranyl tetrachloride and almost no splitting between the lowest non-degenerate (III–IV) states is found. On the other hand, the highest four states (IX–XII) now follow the ordering of the reference calculation for model (d), even though they remain too close to each other. The relative positioning of the intermediate (V–VIII) states among themselves also very much resembles that of the reference. We note that states VII and VIII now come in the same order as in WFT calculations and in experiments. By including the point charges the overall red shift of the spectrum is now about $\approx 3500 \text{ cm}^{-1}$, i.e., only half of that for uranyl.

Model (c), FDE embedding, represents a significant improvement over the point charge approach. The energies of most states approach those of the reference calculation. The most important remaining discrepancy is the position of state IV, which still appears as the lowest excited state. The overall red shift is reduced to about 1000 cm^{-1} and we believe this remaining discrepancies can be attributed to the still too short U–O ground state bond length predicted by this model. If we compare excitation energies relative to the first excited state (columns “rel” in Table 2) we find much better agreement with the reference calculation than for models (a) and (b).

3.2.3 Approximate models, WFT. The above comparison with supermolecular DFT results is useful to assess errors in the embedding approach. However, also with the relatively well-performing CAM-B3LYP functional, TD-DFT cannot capture the subtle correlation effects determining the details of the spectrum, such as the relative order of states VII and VIII. This order is fortuitously corrected in our approximate models whereas the reference model (d) has them in the wrong order compared to the experimental assignment. We will now consider a more advanced treatment of electron correlation. To this end, we begin by addressing the different choices of correlation spaces for the IHFSCSD method.

We present the electronic spectrum of the FDE embedding model (c) for different Q spaces in Table 3, along with IHFSC-112

Table 3 IHFSCSD excitation energies (columns “abs.”) in wavenumbers for the FDE embedding uranyl model (c) without the presence of the crystal environment ($r_{\text{U-O}} = 1.774 \text{ \AA}$), employing different Q spaces (see Table 1). The energies relative to the first excited state are also shown (columns “rel.”)

State	Label (D_{2h})	IHFSCSD-112/ Q_1		IHFSCSD/ Q_1		IHFSCSD/ Q_2		IHFSCSD/ Q_3	
		abs.	rel.	abs.	rel.	abs.	rel.	abs.	rel.
I, II	B_{2g}, B_{3g}	17 998	0	16 896	0	15 746	0	15 680	0
III	B_{1g}	18 705	707	17 624	728	16 432	686	16 365	685
IV	A_g	19 409	1411	18 400	1504	17 116	1370	17 043	1363
V, VI	B_{2g}, B_{3g}	20 689	2691	19 696	2800	18 389	2643	18 318	2637
VII	A_g	21 797	3800	20 834	3938	19 400	3654	19 323	3643
VIII	B_{1g}	21 855	3858	20 915	4019	19 448	3702	19 370	3690
IX, X	B_{2g}, B_{3g}	25 131	7134	24 108	7212	22 805	7059	22 746	7065
XI	B_{1g}	27 602	9604	26 626	9730	25 218	9472	25 155	9475
XII	A_g	27 603	9606	26 628	9732	25 220	9474	25 157	9477

results for the smallest Q space. It is clear that as Q becomes larger, absolute IHFSCSD excitation energies as well as the spacing between adjacent electronic states become smaller, while there are no significant changes in the composition of the states (for further details see Table S7 in the ESI†). Because the smaller Q_2 active space yields results close to the largest space, Q_3 , for both absolute energies and spacings, one can consider the former as sufficiently accurate for evaluating different structural models. Reducing Q_2 further to Q_1 gives errors of about $1200\text{--}1400 \text{ cm}^{-1}$ for absolute energies and up to 300 cm^{-1} for the spacings of higher-lying states. The sensitivity of the outcome to the amount of electron correlation that is included is also visible in the differences between IHFSCSD/ Q_1 and IHFSC-112/ Q_1 , where the spacings between levels and the composition of the states are rather similar but the absolute energies differ by about 1000 cm^{-1} .

Next, we turn to the results of IHFSCSD/ Q_2 calculations on the different approximate models, which can be found in Table 4. As we do not have IHFSCSD results available for uranyl chloride [model (d)], we also list the vertical SO-CASPT2 excitation energies of ref. 19 in Table 4 in order to provide a

Table 4 IHFSCSD/ Q_2 excitation energies (columns “abs.”) in wavenumbers for different uranyl models (a–c) without the presence of the crystal environment ($r_{\text{U-O}} = 1.774 \text{ \AA}$). The energies relative to the first excited state are also shown (columns “rel.”). As there are no IHFSCSD results for uranyl chloride (model d), we include here the vertical SO-CASPT2 excitation energies of Pierloot and van Besien¹⁹ for comparison

State	Label (D_{2h})	Model (a)		Model (b)		Model (c)		Model (d), ^a ref. 19	
		abs.	rel.	abs.	rel.	abs.	rel.	abs.	rel.
I, II	B_{2g}, B_{3g}	12 296		14 757		15 746		21 024	
III	B_{1g}	11 105	−1191	15 132	375	16 432	686	21 273	249
IV	A_g	11 105	−1191	15 421	664	17 116	1370	22 125	1101
V, VI	B_{2g}, B_{3g}	12 303	7	16 620	1863	18 389	2643	22 859	1835
VII	A_g	14 426	2130	17 600	2843	19 400	3654	24 056	3032
VIII	B_{1g}	14 426	2130	17 687	2930	19 448	3702	24 339	3315
IX, X	B_{2g}, B_{3g}	17 593	5297	21 061	6304	22 805	7059	27 494	6470
XI	B_{1g}	17 659	5363	22 829	8072	25 218	9472	29 842	8818
XII	A_g	17 659	5363	22 829	8073	25 220	9474	29 849	8825

^a Vertical SO-CASPT2 results¹⁹ calculated for $r_{\text{U-O}} = 1.783 \text{ \AA}$ and $r_{\text{U-Cl}} = 2.712 \text{ \AA}$.

comparison to a supermolecular WFT calculation. One should, however, focus more on comparing trends for the spectra rather than absolute values for two reasons. First, the SO-CASPT2 calculations were performed for a slightly different geometry ($r_{\text{U-O}} = 1.783 \text{ \AA}$ and $r_{\text{U-Cl}} = 2.712 \text{ \AA}$). From the discussion above as well as from previous studies of uranyl^{21,27} it is apparent that small changes in geometry may correspond to large changes in the vertical excitation energies. Second, there is evidence in the literature^{17,21,27} that CASPT2 consistently places equivalent excitations at higher energies than IHFSCSD for a given geometry, while spacings between excited levels are often in good agreement between the two methods.

As was the case for TD-DFT, we see a steady improvement in the agreement on the absolute excitation energies between the approximate models (a–c) and the reference (d). We observe differences ($\approx 3000\text{--}4000 \text{ cm}^{-1}$) similar to those found for CAM-B3LYP between the bare (a) and point-charge embedded (b) models, and slightly smaller ($\approx 1000\text{--}2000 \text{ cm}^{-1}$) ones between the latter and the FDE model (c). The isolated uranyl model (a) yields once more rather low values for the excitation energies. As for the TD-DFT calculations discussed above, we attributed these differences to the bond length employed here, which is nearly 0.1 \AA larger than the CCSD equilibrium value²⁷ of 1.685 \AA . We observe a qualitative agreement between the IHFSCSD and CAM-B3LYP excitation energies, for instance with the first E_g state higher than the B_{1g} or A_g states, but note that these are typically $\approx 1000 \text{ cm}^{-1}$ lower for IHFSCSD than for the corresponding CAM-B3LYP ones. This agrees with earlier observations.¹⁷ For both the point-charge and FDE embedded models, excitation energies are still red-shifted compared to experiments. Nevertheless, in contrast to CAM-B3LYP, IHFSCSD provides the correct order of the low-lying states.

Furthermore, the spacings between levels are generally larger than those for CAM-B3LYP and are in rather good agreement with the SO-CASPT2 results with the exception of states VII and VIII, which are much closer together for IHFSCSD than for CASPT2. Another interesting difference with respect to CAM-B3LYP is that here models (b) and (c) exhibit differences of similar magnitude relative to the CASPT2 E^{rel} values [$\Delta E_{\text{(b)}}^{\text{rel}} \approx -315 \text{ cm}^{-1}$ and

$\Delta E_{\text{(c)}}^{\text{rel}} \approx 552 \text{ cm}^{-1}$, respectively], but with a standard deviation for $E_{\text{(c)}}^{\text{rel}}$ of about half of that for $E_{\text{(b)}}^{\text{rel}}$ [$\sigma_{\text{(b)}}^{\text{rel}} \approx 306 \text{ cm}^{-1}$ and $\sigma_{\text{(c)}}^{\text{rel}} \approx 163 \text{ cm}^{-1}$, respectively]. For this reason, we think model (c) indeed yields an improvement over (b). That said, the overall agreement with respect to spacings between models (b–d) can be related to a similar composition of the excited states' wavefunctions. To that end, it is instructive to compare the composition of the states (see Tables S6 and S7 in the ESI†) to their analogues in ref. 19. From this comparison, we observe rather similar ratios between the contributions of $\sigma^1\delta^1$ and $\sigma^1\phi^1$ character to the different states for CASPT2 and IHFSCSD. However, for some excitations (e.g. IV, V–VI, IX–X) IHFSCSD gives higher weights to the latter, as well as to $\pi^1\delta^1$ and $\pi^1\phi^1$ configurations.

3.3 Inclusion of the crystal environment

From the discussion above we believe we can consider the FDE embedded uranyl model (c) as a sufficiently accurate representation of the uranyl tetrachloride species (d), and, given the significant differences in computational costs between the two (see Table S1 in the ESI†) as well as the need to use a lower (C_{2h}) symmetry when considering the crystal environment, from now on we only consider FDE embedded UO_2^{2+} models. Our results are presented in Table 5.

We observe that, when passing from an idealized geometry (model c) to the experimental one (model c'), there is little change in the excited states' energies. The only difference is the splitting of the doubly degenerate states in the former (I–II, V–VI and IX–X respectively). In the case of CAM-B3LYP calculations, already at this stage the magnitude of the splitting for the lowest two states matches quite well the experimentally observed one, while for higher states there is an underestimation. Adding the crystal environment brings about a nearly homogeneous stabilization of occupied and virtual orbitals with respect to the isolated uranyl chloride species. Therefore, one sees only relatively small changes in the electronic spectrum for the crystal models.

Model (e), in which the nearest cesium atoms are not relaxed, changes the excitation energies relative to those of model (c') by

Table 5 CAM-B3LYP and IHFSC-112/ Q_1 excitation energies (columns "abs."), in wavenumbers, at the experimental geometry (C_{2h}) for models (c'), (e) and (f). The energies relative to the first excited state are also shown (columns "rel.") for each case

State	Label (D_{2h})	CAM-B3LYP						IHFSC-112/ Q_1							
		Model (c')		Model (e)		Model (f)		Model (c')		Model (f)		Ref. 10		Exp. ref. 31 and 65	
		abs.	rel.	abs.	rel.	abs.	rel.	abs.	rel.	abs.	rel.	abs.	rel.	abs.	rel.
I	B_{2g}	18 114		18 134		18 119		18 151		18 128		20 364		20095.7	
II	B_{3g}	18 112	−2	18 136	2	18 120	1	18 154	3	18 124	−4	20 363	−1	20097.3	1.6
III	B_{1g}	17 975	−139	17 938	−196	17 913	−206	18 874	723	18 816	688	21 013	649	20406.5	310.8
IV	A_g	18 317	203	18 263	129	18 236	117	19 552	1401	19 492	1364	21 838	1474	21316	1220.3
V	B_{2g}	19 568	1454	19 520	1386	19 494	1375	20 836	2685	20 760	2632	22 808	2444	22026.1	1930.4
VI	B_{3g}	19 552	1438	19 501	1367	19 475	1356	20 843	2692	20 768	2640	22 830	2466	22076	1980.3
VII	A_g	20 536	2422	20 514	2380	20 494	2375	21 944	3793	21 848	3720	24 618	4254	22406	2310.3
VIII	B_{1g}	20 825	2711	20 826	2692	20 808	2689	22 005	3854	21 905	3777	24 780	4416	22750	2654.3
IX	B_{2g}	24 749	6635	24 733	6599	24 711	6592	25 297	7146	25 185	7057	26 763	6399	26197.3	6101.6
X	B_{3g}	24 738	6624	24 719	6585	24 698	6579	25 307	7156	25 201	7073	26 871	6507	26247.3	6151.6
XI	B_{1g}	26 131	8017	26 045	7911	26 014	7895	27 779	9628	27 634	9506	29 169	8805	27719.6	7623.9
XII	A_g	26 134	8020	26 048	7914	26 017	7898	27 781	9630	27 637	9509	29 145	8781	27757	7661.3

no more than $\approx 90 \text{ cm}^{-1}$. Generally, it decreases the excitation energies and the largest (in magnitude) changes are observed for the highest states considered. Relaxing the nearest cesiums (model **f**) accentuates this tendency by an additional lowering of about $\approx 23 \text{ cm}^{-1}$. Therefore, we conclude that, as expected, crystal contributions are an order of magnitude smaller than those of the equatorial ligands. The small differential effect from the crystal implies that CAM-B3LYP continues to underestimate the experimental excitation energies by about $1800\text{--}2000 \text{ cm}^{-1}$, as it was the case for model (**d**) discussed above. For the relative spacings between states these small effects captured by the models for the crystal are more significant.

Similar trends are found in the WFT-in-DFT results. We should note, however, that in these calculations it was difficult to converge the coupled cluster amplitudes for the (1h,1p) sector, so that we had to employ exclusively the IHFSCC-112 approximation discussed previously. Due to the increase in computational costs caused by the lower symmetry of the central uranyl unit, we could only employ the Q_1 space. Consequently, the absolute excitation energies in Table 5 are probably overestimating the calculation of IHFSCCSD/ Q_2 quality by about 2000 cm^{-1} for excitations and 100 cm^{-1} for spacings.

The IHFSCC-112 excited states' composition for the uranyl embedded in the chlorides (shown in Table S8 of the ESI[†]) is essentially the same as that in the idealized structure discussed above. In the presence of the crystal environment, we observe that the lowest four states show more equivalent contributions from $\{\sigma^1\delta^1, \pi^1\delta^1\}$ and $\{\sigma^1\phi^1, \pi^1\phi^1\}$ configurations than the isolated models, whereas for higher states the same picture is found for all models.

The only other study which considers the effect of the crystal environment in detail is due to Matsika and Pitzer.¹⁰ They combined a SO-MRCI description of the central uranyl tetrachloride with an embedded cluster model in which pseudopotentials are used to represent the six nearest-neighbor cesium ions, while the Madelung potential arising from the rest of the crystal was represented by an array of point charges. Compared to these results, the CAM-B3LYP calculations better describe the excited state spacings for all but the third and fourth excited states. On the other hand, the results obtained with Fock-space are generally of similar quality to the SO-MRCI ones, with better agreement with the experimental results for some of the lower states, but with a strong underestimation of the energy difference between states VII and VIII.

As we can establish from our models that interactions between the central uranyl chloride unit and further species are relatively small, the main source of errors in our calculations is then likely to be due to the treatment of electron correlation. There, we observe that neither CAM-B3LYP nor any of the *ab initio* approaches employed so far to investigate $\text{Cs}_2\text{UO}_2\text{Cl}_4$ or the bare uranyl chloride species are able to achieve "spectroscopic" accuracy for the absolute excitation energies of $\text{Cs}_2\text{UO}_2\text{Cl}_4$, by which we mean discrepancies between theory and experiment of $\approx 50\text{--}100 \text{ cm}^{-1}$ for the low-lying transitions (due to the extremely good resolution of the experimental data). This underscores both the difficulty of determining such spectra

from first principles and the need to investigate the performance of higher accuracy methods (*e.g.* those including triple or higher excitations explicitly) which, albeit too costly to be employed in routine calculations, might nevertheless provide insight into the factors controlling the accuracy of more widely applicable approaches (*e.g.* DFT, CASPT2 or IHFSCCSD) and help devise more efficient and accurate approximations.

3.4 A closer look at the occupied spinors

Apart from the analysis of the optical spectra above, it is also instructive to compare orbital energies between the models to gauge the accuracy of the embedding. Furthermore, the occupied orbital energies can be compared with experimental studies of ionization energies.

3.4.1 Uranyl (chloride) in the gas phase. We start with CAM-B3LYP, for which we show in Table 6 the orbital energies (ϵ , in eV) for the valence region ($-\epsilon < 6 \text{ eV}$) for models (**c**) and (**d**). Here we note that for the FDE-embedded model (**c**), we have orbital energies for both the UO_2^{2+} and Cl_4^{4-} subsystems because of the employed freeze-and-thaw procedure. We see a very good agreement for the outer orbitals between the two models. In particular, the HOMO energy for model (**d**) agrees closely with the one of the Cl_4^{4-} fragment in model (**c**). This is understandable, since calculations on uranyl tetrachloride identify the HOMO essentially as a ligand orbital. Therefore, both models can yield approximations of similar quality to the molecule's first ionization potential,⁹⁶ with 1.78 eV and 1.72 eV for models (**c**) and (**d**) respectively. These are significantly smaller than the recent gas-phase experimental vertical electron detachment (ED) energy of 2.62 eV,⁷¹ and reflect the fact that DFT calculations can strongly underestimate this quantity.¹⁷

Discrepancies between the calculations for the two models become larger for the region between -2.5 and 5.0 eV . In this region, one starts to see spinors with both chloride and uranyl contributions in model (**d**), whereas such direct mixing is

Table 6 CAM-B3LYP orbital energies (ϵ , in eV) for the valence region for models (**c**) and (**d**) in the idealized (D_{4h}) structure and the difference between the two ($\Delta\epsilon$)

Label	Model (c)		Model (d)	
	$-\epsilon$	Fragment	$-\epsilon$	$\Delta\epsilon$
e_{1g}	1.78	Cl_4^{4-}	1.72	0.06
e_{1u}	2.09	Cl_4^{4-}	1.90	0.19
e_{1g}	2.26	Cl_4^{4-}	1.97	0.29
e_{1g}	2.27	Cl_4^{4-}	1.97	0.30
e_{1u}	2.13	Cl_4^{4-}	2.10	0.03
e_{1u}	2.16	Cl_4^{4-}	2.24	-0.08
e_{1u}	2.45	Cl_4^{4-}	2.32	0.13
e_{1u}	3.39	Cl_4^{4-}	2.35	1.04
e_{1u}	3.44	Cl_4^{4-}	2.61	0.83
e_{1g}	2.55	Cl_4^{4-}	3.07	-0.52
e_{1g}	2.81	Cl_4^{4-}	3.26	-0.45
e_{1g}	4.78	Cl_4^{4-}	3.52	1.26
e_{1u}	4.24	UO_2^{2+}	3.70	0.54
e_{1u}	4.93	UO_2^{2+}	4.23	0.70
e_{1u}	5.33	UO_2^{2+}	4.49	0.84
e_{1g}	5.38	UO_2^{2+}	4.90	0.48
e_{1g}	5.38	UO_2^{2+}	5.01	0.37
e_{1g}	5.49	UO_2^{2+}	5.09	0.40

Table 7 CAM-B3LYP (columns a), IHFSCSD/ Q_2 (columns b) and IHFSCSD/ Q_1 (columns c) absolute ionization energies (in eV) for different models for embedded uranyl

	Model (b)		Model (c)			Model (f)	
	(a)	(b)	(a)	(b)	(c)	(a)	(c)
e_{1u}	6.16	7.78	4.24	5.81	5.51	9.32	10.61
e_{1u}	6.78	8.14	4.93	6.21	6.01	9.99	11.08
e_{1u}	7.15	8.54	5.33	6.63	6.31	10.40	11.50
e_{1g}	7.10	8.32	5.38	6.56	6.40	10.41	11.50
e_{1g}	7.13	8.46	5.38	6.65	6.50	10.47	11.54
e_{1g}	7.23	8.56	5.49	6.75	6.59	10.56	11.67

absent by construction in model (c). Nevertheless, we observe a good agreement between the supermolecule (3.7 eV) or FDE results (4.2 eV) for the highest uranyl-dominated orbital. Moreover, this is close to the attributed vertical ED energy for the experimental uranyl-dominated spinors⁷¹ at about 5 eV. In contrast, the corresponding uranyl ionization energy derived with the point-charge embedding of 6.2 eV, shown in Table 7, is significantly higher.

The IHFSCSD results for the uranyl ionization energies in the FDE and point-charge models (b) and (c), also shown in Table 7, follow a similar trend. There is a strong overestimation in the point-charge model (7.78 eV) compared to FDE (5.81 eV), which gives values in good agreement with experiments. The many-electron ED states are essentially dominated by single determinants so that one can associate those to the ionizations of the individual Hartree–Fock spinor stabilized by correlation effects of the order of 1 eV. The effect of the completeness of the Q space is again not negligible and amounts to about 0.3 eV.

3.4.2 Uranyl in $Cs_2UO_2Cl_4$. Our results for the crystal model in which we allow the nearest Cs^+ ions to be polarized (model f) are also included in Table 7. Due to the effect of the Madelung potential, we observe a marked increase (about 5 eV) in the ionization energies for the uranyl electrons, compared to the corresponding isolated uranyl chloride models. Furthermore, we now have the three e_g levels in the valence more stable than the e_u ones for both CAM-B3LYP and IHFSCSD.

The results for the first ionization energy are in good agreement with an experimental estimate⁶⁵ which places the binding energy of the valence uranyl electrons at about 9.4 eV. Compared to that value, CAM-B3LYP shows only a slight underestimation, while IHFSCSD would appear to overestimate it by about 1 eV. However, in our calculations the polarization of the surroundings that would occur after the removal of an electron – which would provide a net stabilization of the final state – is not taken into account. Therefore, one can expect that once these are included, CAM-B3LYP would yield too low ionization potentials, in line with its known tendency to underestimate the ionization energies,¹⁷ whereas IHFSCSD would approach the experimental values.

4 Conclusions

We have investigated the electronic structure and spectra in the UV-Visible range of the uranyl cation (UO_2^{2+}) in $Cs_2UO_2Cl_4$,

employing subsystem embedding approaches (DFT-in-DFT and WFT-in-DFT), in order to construct models of increasing sophistication for the crystal environment.

We have found that with the FDE formalism one can construct models in which the equatorial ligands to the uranyl species are represented in an approximate fashion as an embedding potential. The electronic spectra of such approximate models are able to capture, without significant loss of accuracy, the spectral features (spacing between states, symmetry classification) of the uranyl tetrachloride molecule for states that do not exhibit LMCT character, as well as its first ionization potential.

These models were further applied in calculations taking into account the crystal environment beyond the chloride ligands. As found in our prior investigation of NpO_2^{2+} as an impurity in $Cs_2UO_2Cl_4$, at the experimental geometry we see rather small contributions due to the frozen crystal environment, which are larger for higher-lying states than for lower-lying ones. The relaxation of the electron density for atoms in the immediate vicinity of the central uranyl tetrachloride species accentuates this tendency, and turns out to be significant for describing the states' relative positions with respect to experiments. As the most significant environment effects are due to the presence of the equatorial ligands, the common practice in the literature, which consists of considering the isolated uranyl tetrachloride species, is indeed justified and a very good model for the spectrum in condensed phase.

The overall good performance of our embedded uranyl model makes us confident in applying such models to investigate the spectrum of uranyl in other condensed media and in the presence of different ligands. Nevertheless, these approximate models yield spectra which are on the whole red shifted. From our results and those available in the literature, we have concluded that these shifts can be attributed to a tendency of the approximate models to yield U–O equilibrium bond lengths which are shorter than the experimental ones. Thus, our calculations would in fact be sampling a region of the potential energy curves where the ground and excited states are starting to coalesce. We plan to investigate this issue further. We also plan to investigate the extent to which one can employ subsystem approaches to define minimalistic models for other classes of actinide-containing molecules (*e.g.* not containing the actinyl species, and where ligand–actinide interactions are more covalent than those investigated here) which can still yield accurate electronic spectra in the optical range.

In addition to an assessment of physical models, our results also provide further evidence for the applicability of the CAM-B3LYP functional to describe the electronic structure of actinyl-containing species, while at the same time underscoring the difficulty of all *ab initio* approaches employed so far to obtain very accurate energies for the low-lying electronic states of $Cs_2UO_2Cl_4$.

Acknowledgements

This study was supported by the EC-supported ACTINET-i3 Integrated Infrastructure Initiative (JRP-C3-10, JRP-C5-08). ASPG, FR and

VV acknowledge support from PhLAM (Laboratoire de Physique des Lasers, Atomes et Molécules, Unité Mixte de Recherche de l'Université du CNRS), as well as the use of HPC resources from GENCI-CCRT (Grants 2012-081859 and 2013-081859). LV acknowledges the financial support from The Netherlands Organization for Scientific Research (NWO) via the Vici and NCF (computer time) programs. C.R.J. acknowledges support from the DFG-Center for Functional Nanostructures.

References

- 1 F. J. C. Rossotti and H. Rossotti, *The Determination of Stability Constants*, McGraw-Hill, New York, 1961.
- 2 V. Eliet, I. Grenthe and G. Bidoglio, *J. Chem. Soc., Faraday Trans.*, 1995, **91**, 2275–2285.
- 3 P. Lindqvist-Reis, C. Walther, R. Klenze and N. M. Edelstein, *J. Phys. Chem. C*, 2009, **113**, 449–458.
- 4 G. K. Liu, *J. Phys. Chem. A*, 2011, **115**, 12419–12425.
- 5 G. K. Liu, *J. Phys. Chem. A*, 2012, **116**, 7443.
- 6 G. Schreckenbach and G. A. Shamov, *Acc. Chem. Res.*, 2010, **43**, 19.
- 7 T. Fleig, *Chem. Phys.*, 2011, **124**, 104106.
- 8 M. Dolg and X. Cao, *Chem. Rev.*, 2012, **112**, 403.
- 9 S. Matsika, Z. Zhang, S. R. Brozell, J.-P. Blaudeau, Q. Wang and R. M. Pitzer, *J. Phys. Chem. A*, 2001, **105**, 3825.
- 10 S. Matsika and R. M. Pitzer, *J. Phys. Chem. A*, 2001, **105**, 637–645.
- 11 T. Yang, R. Tyagi, Z. Zhang and R. M. Pitzer, *Mol. Phys.*, 2009, **107**, 1193.
- 12 Z. Zhang and R. M. Pitzer, *J. Phys. Chem. A*, 1999, **103**, 6880.
- 13 T. Fleig, H. J. A. Jensen, J. Olsen and L. Visscher, *J. Chem. Phys.*, 2006, **124**, 104106.
- 14 T. Privalov, P. Macak, B. Schimmelpfennig, E. Fromager, I. Grenthe and U. Wahlgren, *J. Am. Chem. Soc.*, 2004, **126**, 9801.
- 15 E. Fromager, F. Real, P. Wahlin, U. Wahlgren and H. J. A. Jensen, *J. Chem. Phys.*, 2009, **131**, 054107.
- 16 F. Ruipérez and U. Wahlgren, *J. Phys. Chem. A*, 2010, **114**, 3615–3621.
- 17 P. Tecmer, A. S. P. Gomes, U. Ekström and L. Visscher, *Phys. Chem. Chem. Phys.*, 2011, **13**, 6249.
- 18 P. Tecmer, R. Bast, K. Ruud and L. Visscher, *J. Phys. Chem. A*, 2012, **116**, 7397–7404.
- 19 K. Pierloot and E. van Besien, *J. Chem. Phys.*, 2005, **123**, 204309.
- 20 K. Pierloot, E. van Besien, E. van Lenthe and E. J. Baerends, *J. Chem. Phys.*, 2007, **126**, 194311.
- 21 F. Réal, V. Vallet, C. Marian and U. Wahlgren, *J. Chem. Phys.*, 2007, **127**, 214302.
- 22 I. Infante, M. Vilkas, I. Ishikawa, U. Kaldor and L. Visscher, *J. Chem. Phys.*, 2007, **127**, 124308.
- 23 I. Infante and L. Visscher, *J. Chem. Phys.*, 2004, **121**, 5783.
- 24 I. Infante, L. Andrews, X. Wang and L. Gagliardi, *Chem.–Eur. J.*, 2010, **16**, 12804.
- 25 L. Andrews, X. Wang, B. Liang, F. Ruipérez, I. Infante, A. D. Raw and J. A. Ibers, *Eur. J. Inorg. Chem.*, 2011, 4457–4463.
- 26 I. Infante, A. S. P. Gomes and L. Visscher, *J. Chem. Phys.*, 2006, **125**, 074301.
- 27 F. Réal, A. S. P. Gomes, L. Visscher, V. Vallet and E. Eliav, *J. Phys. Chem. A*, 2009, **113**, 12504.
- 28 I. Infante, A. Kovacs, G. L. Macchia, A. R. M. Shahi, J. K. Gibson and L. Gagliardi, *J. Phys. Chem. A*, 2010, **114**, 6007.
- 29 G. L. Macchia, I. Infante, J. Raab, J. K. Gibson and L. Gagliardi, *Phys. Chem. Chem. Phys.*, 2008, **48**, 7278.
- 30 R. Bast, H. J. A. Jensen and T. Saue, *Int. J. Quantum Chem.*, 2009, **109**, 2091.
- 31 R. G. Denning, *J. Phys. Chem. A*, 2007, **111**, 4125–4143.
- 32 G. Geipel, *Coord. Chem. Rev.*, 2006, **250**, 844–854.
- 33 L. S. Natrajan, *Coord. Chem. Rev.*, 2012, **256**, 1583–1603.
- 34 K. E. Knope and L. Soderholm, *Chem. Rev.*, 2012, **113**, 944–994.
- 35 C. Danilo, V. Vallet, J.-P. Flament and U. Wahlgren, *Phys. Chem. Chem. Phys.*, 2010, **12**, 1116–1130.
- 36 D. J. Tozer, *J. Chem. Phys.*, 2003, **119**, 12697.
- 37 O. Gritsenko and E. J. Baerends, *J. Chem. Phys.*, 2004, **121**, 655.
- 38 S. Kümmel and L. Kronin, *Rev. Mod. Phys.*, 2008, **80**, 3.
- 39 A. M. Teale, F. D. Proft and D. J. Tozer, *J. Chem. Phys.*, 2008, **129**, 044110.
- 40 T. Yanai, D. P. Tew and N. C. Handy, *Chem. Phys. Lett.*, 2004, **393**, 51–57.
- 41 A. S. P. Gomes and C. R. Jacob, *Annu. Rep. Prog. Chem., Sect. C*, 2012, **108**, 222–277.
- 42 T. A. Wesolowski and A. Warshel, *J. Phys. Chem.*, 1993, **97**, 8050.
- 43 T. A. Wesolowski and J. Weber, *Chem. Phys. Lett.*, 1996, **248**, 71.
- 44 Ch. R. Jacob, J. Neugebauer and L. Visscher, *J. Comput. Chem.*, 2008, **29**, 1011–1018.
- 45 C. R. Jacob and L. Visscher, *J. Chem. Phys.*, 2008, **128**, 155102.
- 46 S. Laricchia, E. Fabiano and F. Della Sala, *J. Chem. Phys.*, 2013, **138**, 124112.
- 47 J. Neugebauer, Ch. R. Jacob, T. A. Wesolowski and E. J. Baerends, *J. Phys. Chem. A*, 2005, **109**, 7805–7814.
- 48 J. Neugebauer, M. J. Louwerse, E. J. Baerends and T. A. Wesolowski, *J. Chem. Phys.*, 2005, **122**, 094115.
- 49 J. Neugebauer and E. J. Baerends, *J. Phys. Chem. A*, 2006, **110**, 8786–8796.
- 50 N. Govind, Y. A. Wang, A. J. R. da Silva and E. Carter, *Chem. Phys. Lett.*, 1998, **295**, 129.
- 51 N. Govind, Y. A. Wang and E. A. Carter, *J. Chem. Phys.*, 1999, **110**, 7677.
- 52 P. Huang and E. A. Carter, *J. Chem. Phys.*, 2006, **125**, 084102.
- 53 A. S. P. Gomes, C. R. Jacob and L. Visscher, *Phys. Chem. Chem. Phys.*, 2008, **10**, 5353.
- 54 S. Höfener and L. Visscher, *J. Chem. Phys.*, 2012, **137**, 204120.
- 55 C. Daday, C. König, O. Valsson, J. Neugebauer and C. Filippi, *J. Chem. Theory Comput.*, 2013, **9**, 2355–2367.
- 56 J. Neugebauer, *J. Chem. Phys.*, 2007, **126**, 134116.
- 57 J. Neugebauer, *J. Chem. Phys.*, 2009, **131**, 084104.
- 58 J. Neugebauer, *J. Phys. Chem. B*, 2008, **112**, 2207–2217.

- 59 S. Höfener, A. S. P. Gomes and L. Visscher, *J. Chem. Phys.*, 2012, **136**, 044104.
- 60 J. Neugebauer, *Phys. Rep.*, 2010, **489**, 1–87.
- 61 C. König and J. Neugebauer, *Phys. Chem. Chem. Phys.*, 2011, **13**, 10475.
- 62 C. König and J. Neugebauer, *ChemPhysChem*, 2012, **13**, 386–425.
- 63 P. Tecmer, H. van Lingen, A. S. P. Gomes and L. Visscher, *J. Chem. Phys.*, 2012, **137**, 084308.
- 64 K. Takao, T. J. Bell and Y. Ikeda, *Inorg. Chem.*, 2013, **53**, 3459–3472.
- 65 R. G. Denning, *Struct. Bonding*, 1992, **79**, 215–276.
- 66 C. D. Flint and P. A. Tanner, *J. Chem. Soc., Faraday Trans. 2*, 1978, **74**, 2210–2217.
- 67 P. A. Tanner, C. S. K. Mak, Z. W. Pei, Y. L. Liu and L. Jun, *J. Phys.: Condens. Matter*, 2001, **13**, 189–194.
- 68 C. Görrler-Walrand and L. G. Vanquickenborne, *J. Chem. Phys.*, 1973, **2**, 360.
- 69 C. Görrler-Walrand, S. De Houwer, L. Fluyt and K. Binnemans, *Phys. Chem. Chem. Phys.*, 2004, **6**, 3292–3298.
- 70 K. Servaes, C. Hennig, R. VanDeun and C. Görrler-Walrand, *Inorg. Chem.*, 2005, **44**, 7705–7707.
- 71 P. D. Dau, J. Su, H.-T. Liu, D.-L. Huang, J. Li and L.-S. Wang, *J. Chem. Phys.*, 2012, **137**, 064315.
- 72 E. van Besien, K. Pierloot and C. Görrler-Walrand, *Phys. Chem. Chem. Phys.*, 2006, **8**, 4311–4319.
- 73 D. J. Watkin, R. G. Denning and K. Prout, *Acta Crystallogr.*, 1991, **C47**, 2517.
- 74 DIRAC, a relativistic *ab initio* electronic structure program, Release DIRAC11 (2011), written by R. Bast, H. J. Aa. Jensen, T. Saue and L. Visscher, with contributions from V. Bakken, K. G. Dyall, S. Dubillard, U. Ekström, E. Eliav, T. Enevoldsen, T. Fleig, O. Fossgaard, A. S. P. Gomes, T. Helgaker, J. K. Lærdahl, J. Henriksson, M. Iliaš, Ch. R. Jacob, S. Knecht, C. V. Larsen, H. S. Nataraj, P. Norman, G. Olejniczak, J. Olsen, J. K. Pedersen, M. Pernpointner, K. Ruud, P. Salek, B. Schimmelpfennig, J. Sikkema, A. J. Thorvaldsen, J. Thyssen, J. van Stralen, S. Villaume, O. Visser, T. Winther and S. Yamamoto (see <http://dirac.chem.vu.nl>).
- 75 K. G. Dyall, *Theor. Chem. Acc.*, 2007, **491**, 483.
- 76 T. H. Dunning, *J. Chem. Phys.*, 1989, **90**, 1007.
- 77 L. Visscher, *Theor. Chem. Acc.*, 1997, **98**, 68.
- 78 L. Visscher, E. Eliav and U. Kaldor, *J. Chem. Phys.*, 2001, **115**, 9720.
- 79 A. Landau, E. Eliav, Y. Ishikawa and U. Kaldor, *J. Chem. Phys.*, 2000, **113**, 9905.
- 80 A. Landau, E. Eliav, Y. Ishikawa and U. Kaldor, *J. Chem. Phys.*, 2001, **115**, 6862.
- 81 A. Landau and E. Eliav, *J. Chem. Phys.*, 2000, **115**, 6862.
- 82 ADF2012.01, SCM, Theoretical Chemistry, Vrije Universiteit, Amsterdam, The Netherlands, <http://www.scm.com>.
- 83 C. R. Jacob, S. M. Beyhan, R. E. Bulo, A. S. P. Gomes, A. W. Götz, K. Kiewisch, J. Sikkema and L. Visscher, *J. Comput. Chem.*, 2011, **32**, 2328.
- 84 E. van Lenthe, E. J. Baerends and J. G. Snijders, *J. Chem. Phys.*, 1993, **99**, 4597.
- 85 E. van Lenthe, E. J. Baerends and J. G. Snijders, *J. Chem. Phys.*, 1994, **101**, 9783.
- 86 E. van Lenthe and E. J. Baerends, *J. Comput. Chem.*, 2003, **24**, 1142.
- 87 P. R. T. Schipper, O. V. Gritsenko, S. J. A. van Gisbergen and E. J. Baerends, *J. Chem. Phys.*, 2000, **112**, 1344–1352.
- 88 O. V. Gritsenko, P. R. T. Schipper and E. J. Baerends, *Chem. Phys. Lett.*, 1999, **302**, 199–207.
- 89 O. V. Gritsenko, P. R. T. Schipper and E. J. Baerends, *Int. J. Quantum Chem.*, 2000, **76**, 407–419.
- 90 J. P. Perdew, in *Electronic Structure of Solids*, ed. P. Ziesche and H. Eschrig, Akademie Verlag, Berlin, 1991, pp. 11–20.
- 91 A. Lembarki and H. Chermette, *Phys. Rev. A: At., Mol., Opt. Phys.*, 1994, **50**, 5328.
- 92 A. Gelle and M.-B. Lepetit, *J. Chem. Phys.*, 2008, **128**, 244716.
- 93 V. V. Zhurov, E. A. Zhurova, A. I. Stash and A. A. Pinkerton, *J. Phys. Chem. A*, 2011, **115**, 13016–13023.
- 94 V. Vallet, U. Wahlgren and I. Grenthe, *J. Phys. Chem. A*, 2012, **116**, 12373–12380.
- 95 S. A. Kozimor, P. Yang, E. R. Batista, K. S. Boland, C. J. Burns, D. L. Clark, S. D. Conradson, R. L. Martin, M. P. Wilkerson and L. E. Wolfsberg, *J. Am. Chem. Soc.*, 2009, **131**, 12125–12136.
- 96 D. P. Chong, O. V. Gritsenko and E. J. Baerends, *J. Chem. Phys.*, 2002, **117**, 1760.